PCCP

ROYAL SOCIETY OF CHEMISTRY

PAPER

View Article Online
View Journal | View Issue

Cite this: *Phys. Chem. Chem. Phys.*, 2024, **26**, 29887

Mechanistic insights into CO_2 reduction to CO by group 5 transition metal monoxide cations†

Haili Yu,‡[a] Jia Han,‡*[b] Quyan Su,[a] Pengcheng Liu,[c] Shilin Liu[ab] and Xiaoguo Zhou*[ab]

Received 21st August 2024,
Accepted 22nd November 2024

DOI: 10.1039/d4cp03278k

rsc.li/pccp

The reduction of carbon dioxide (CO_2) by transition-metal oxides in the gas phase serves as a unique model system for understanding transition metal-based catalytic systems in CO_2 utilization. In this work, thermochemistry and reaction mechanisms attributed to the two-state reactivity scenario of CO_2 reduction by group 5 transition metal monoxide cations are extensively investigated using quantum chemical calculations. The interaction between the VO^+ cation with CO_2 exhibits an endothermic feature, whereas the reaction involving the TaO^+ cation showcases a more pronounced exothermic behavior than the NbO^+ cation, in accordance with previously reported reaction rates. Based on in-depth examinations of potential energy surfaces and spin–orbit couplings, it has been revealed that the reaction kinetics of CO_2 reduction to CO by the VO^+ cation is restricted not only by a significant energy barrier related to the singlet transition state, but also by the limited probability of intersystem crossing. For NbO^+ and TaO^+ cations, the spin inversion from triplet to singlet pathways becomes the rate-limiting step. The reaction with the TaO^+ cation represents a different case from typical two-state reactivity patterns, where the minimum energy crossing point submerged relative to the reactants level stands for the exclusive barrier. A considerably higher probability of intersystem crossing was identified for the reaction of the TaO^+ cation with CO_2, elucidating the basis for the substantial increase in the rate constant compared to that of the NbO^+ cation.

1. Introduction

The progressive increase of CO_2 concentration in the atmosphere and the harmful environmental impacts of this greenhouse gas have prompted tremendous efforts to reduce CO_2 emissions.[1–3] In this context, the catalytic conversion of CO_2 into value-added chemicals and feedstocks has emerged as a promising strategy to mitigate the global warming phenomenon and meet global energy demands. CO_2 utilization based on photochemical, biochemical and electrochemical processes has been innovatively developed and applied as a broad strategy to balance out the atmospheric carbon levels from the last several decades.[4–12] In general, photochemical transformation of CO_2 utilizes light irradiation to drive the thermodynamic reactions, while biochemical conversion involves enzymatic processes and electrochemical reduction of CO_2 requires electric energy for the generation of carbon-based chemical products.[13] Compared to those technologies, chemical conversion of CO_2 into its reduced forms presents more challenges due to the significant energy required for the C=O bond cleavage in the absence of any external potential.[14,15] Therefore, one of the main research goals in achieving the efficient transformation of this stable molecule is its activation and reduction by suitable catalysts.

Two distinct directions have emerged in the development of catalysts that are capable of facilitating the reduction of CO_2. One major project focuses on the conversion of CO_2 into formic acid, formaldehyde and methanol through hydrogenation.[16] Nevertheless, precisely controlling the extent of reduction upon H_2 addition in the reactions has proven to be intricate, which hinders selective production. Moreover, it is essential to sustainably produce the reducing reagents on a large scale.[17,18] Another attractive strategy is the catalytic conversion of CO_2 into CO, which can be used as a feedstock for downstream methanol production and Fischer–Tropsch synthesis.[19,20]

Transition metal-based species have been the focus of extensive research due to their crucial role in converting CO_2 molecules to CO, in which these interactions serve as well-defined models of coordinately unsaturated active sites on

[a] *Department of Chemical Physics, University of Science and Technology of China, Hefei 230026, China. E-mail: xzhou@ustc.edu.cn*
[b] *Hefei National Research Center for Physical Sciences at the Microscale, University of Science and Technology of China, Hefei 230026, China. E-mail: jiahan@ustc.edu.cn*
[c] *Anhui Institute of Optics and Fine Mechanics, Hefei Institutes of Physical Science, Chinese Academy of Sciences, Hefei 230031, China*

† Electronic supplementary information (ESI) available. See DOI: https://doi.org/10.1039/d4cp03278k

‡ These authors contributed equally to this work.

catalyst surfaces upon CO_2 adsorption.[21,22] The reactions of transition metals as well as oxides and CO_2 have been extensively studied in the past. For example, Matrix isolation FTIR spectroscopic studies in cryogenic gas matrices indicated that early transition metal atoms (Sc, Ti, V, Cr, Y and Zr) are able to spontaneously insert into the C═O bond, yielding oxocarbonyl species.[23–25] Considering the charge transfer processes at the catalyst-support interface, the role of transition metal atoms with different charge states has also been comprehensively investigated in the gas phase, aiming to improve mechanistic understandings of catalytic reactions on the surface. In a thorough experimental survey, the thermodynamic and kinetic information of the reactions between CO_2 and 46 metal cations at room temperature have been revealed by Koyanagi and Bohme.[26] Nine early transition metal cations (Sc^+, Y^+, La^+, Ti^+, Zr^+, Hf^+, Nb^+, Ta^+ and W^+), possessing oxygen affinities (OAs) greater than OA(CO) = 526 kJ mol^{-1}, were reported to be able to reduce CO_2 molecules through oxygen atom abstraction in an exothermic fashion (Reaction (1)).[27] In particular, no detection of the formation of VO^+ and VO_2^+ cations *via* oxygen atom abstraction has been made, despite the shared exothermic nature of the ion–molecule reactions between CO_2 molecules and the group 5 transition metal cations.[26,28] Earlier collision-induced dissociation (CID) by the Armentrout group has investigated the kinetic behaviors of spin-forbidden reactions between transition metal oxide cations and CO_2, demonstrating that these reactions are only thermodynamically feasible when the bond dissociation energies of the newly formed metal oxides exceed those of the C═O bonds in CO_2.[29–32] Similarly, Beauchamp studied guided ion beam activation of transition metal cations to activate C–H bonds and found a correlation between the activation capacity and the spin state of the transition metal cation.[33–37] Therefore, both thermodynamics and spin jumps play significant roles in the reduction of CO_2 molecules, particularly in the conversion from high-spin M^+ cation to lower-spin MO^+ cation.[38] Although the spin-controlled reactions involving transition metals have been extensively explored, recent machine learning studies by Liu and colleagues have created full-dimensional potential energy surfaces for the Ta^+ and CO_2 two-state reactions.[39] This advancement provides deeper insights into the dynamics of these non-adiabatic reactions, revealing that intersystem crossover primarily drives the kinetic behavior, rather than potential energy control. Thus, we can infer that the limited reactivity of the V^+ cation suggests a kinetic barrier that probably arises from an inefficient surface crossing between different ground electronic states of the reactants and products.

$$M^+ + CO_2 \rightarrow MO^+ + CO \quad (1)$$

$$MO^+ + CO_2 \rightarrow MO_2^+ + CO \quad (2)$$

Based on the previous results of Koyanagi and Bohme, of these nine cations only four, *i.e.* Hf^+, Nb^+, Ta^+ and W^+, were observed to form dioxide cations *via* sequential oxygen atom abstraction (Reaction (2)).[26] This reaction experienced an exceptionally slow process with the HfO^+ cation. On the other hand, NbO^+, TaO^+ and WO^+ cations were found to reduce CO_2 molecules at markedly different reaction rates of about 2 orders of magnitude, despite having similar bond dissociation energies D_0(O–MO^+). However, the mechanisms and the rate-determining factors of CO_2 reduction by transition metal oxide cations remain largely unknown.

In this study, we present detailed and comprehensive theoretical investigations on the mechanisms of gas-phase reactions of CO_2 molecules with the group 5 transition metal monoxide cations, with the objective of evaluating their periodic variations in reaction kinetics from both thermodynamic and spin change perspectives. Understanding the underlying mechanisms and uncovering the controlling factors of reaction rates and efficiencies provide valuable insights into the fundamental processes involved in CO_2 reduction by transition metal-based catalytic systems, which further contributes to the optimization and development of efficient catalysts for CO_2 conversion.

2. Computational method

Quantum chemical calculations were performed to investigate the mechanisms governing the reactions of MO^+ (M = V, Nb, Ta) cations with CO_2 molecules. First, a large number of different isomers for the $[OM\cdots CO_2]^+$ complex were randomly generated by Genmer.[40] The geometries were initially pre-optimized using the semi-empirical quantum mechanical method GFN2-*x*TB with the xtb program.[40,41] Further optimization of the low-lying structures was carried out using the PBE0 functional augmented with dispersion correcting PBE0-D3(BJ) with the def2-TZVP basis set for all the elements.[42,43] Vibrational frequencies were calculated at the same density functional level to ensure that all found minima have no imaginary frequencies and transition states exhibit only one imaginary frequency. Intrinsic reaction coordinate (IRC) calculations were conducted to confirm that each reported transition state connects two appropriate minima.[44–47] All the density functional calculations were carried out with the Gaussian 16 software package.[48] For each optimized geometry, higher level single-point energies were evaluated at the U/UCCSD(T)/def2-QZVPP level of theory using the ORCA suite of program.[49–53]

The minimum energy crossing points (MECPs) between potential energy surfaces corresponding to different spin states were located by the sobMECP method, a modified version of Harvey's MECP program.[54,55] At the MECPs the transition probability between the singlet and triplet spin states is computed by using Landau–Zener formula[56,57]

$$P^{ISC} = 1 - \exp\left(\frac{-4\pi^2 {H_{SOC}}^2}{h\nu|\Delta g|}\right) \quad (3)$$

where H_{SOC} is the spin–orbit coupling (SOC) constant and $|\Delta g|$ is the norm of the difference of the gradients on the two surfaces at the MECP and ν is the velocity of the system also the MECP. The velocity ν can be approximated by the average

Table 1 Bond dissociation energies, $D_0(OM^+–O)$ at 0 K (in kJ mol^{-1}), for ground-state MO_2^+ (M = V, Nb, Ta) cations calculated at the PBE0-D3(BJ)/def2-TZVP and U/UCCSD(T)/def2-QZVPP levels of theory and some literature data given for comparison

	Present		Previous	
$D_0(OM^+–O)$	PBE0	U/UCCSD(T)	Exp.(method)	Theo.(method)
$OV^+–O$	496	421	295 ± 39(CID)[a]	357(B3LYP/TZV)[c]
			339 ± 35(CID)[b]	377(B3LYP/BSII)[d]
$ONb^+–O$	546	580	551 ± 16(CID)[e]	530(B3LYP/BSII)[d]
				572(CCSD(T)/QZVPPD)[f]
$OTa^+–O$	568	594	587 ± 12(CID)[g]	596(CCSD(T)/QZVPPD)[f]

[a] Ref. 29. [b] Ref. 71. [c] Ref. 72. [d] Ref. 73. [e] Ref. 30. [f] Ref. 74. [g] Ref. 68.

velocity obtained from the unidimensional Maxwell–Boltzmann distribution:

$$v = \left(\frac{3k_B T}{\mu}\right)^2 \quad (4)$$

where k_B is the Boltzmann constant T is the temperature and μ is the reduced mass.

The spin–orbit coupling constants of the MECPs were calculated by using the complete active space self-consistent field (CASSCF) method with second-order *N*-electron valence state perturbation theory (NEVPT2).[40,58–61] The Scalar relativistic effects utilize the Douglas–Kroll–Hess approximation, we use the all-electronic SARC-DKH-TZVP basis set for Nb and Ta atoms, and the DKH-adapted version of the def2-TZVP basis set for O, C, and V atoms.[62–64] An active space of CAS (10e, 12o) is used, which includes 3d and 4s shells for the V atom, 4d and 5s shells for the Nb atom, 5d and 6s shells for the Ta atom, as well as 2p shells for the C and O atoms. This active space is selected based on the composition of the highest singly occupied molecular orbital (SOMO) and SOMO-1 orbitals involved in the spin–flip processes, as calculated within the framework of the restricted open-shell Hartree–Fock (ROHF) theory. All SOC calculations were performed with the ORCA program.[49,50] The frontier molecular orbital analysis the natural atomic orbital (NAO) analysis was carried out using Multiwfn program.[65–67]

3. Results and discussion

3.1. Thermochemistry of CO_2 reduction to CO by MO^+ (M = V, Nb, Ta) cations

In accordance with previous studies, the ground electronic states of MO^+ and MO_2^+ (M = V, Nb, Ta) cations were theoretically determined to be the triplet state and the singlet state, respectively (Fig. S1, ESI†).[29,31,68] Therefore, a two-state reactivity scenario can be expected.[69,70] The activation of the C═O bond by VO^+, NbO^+ and TaO^+ cations may follow a similar pattern as CO_2 reduction by atomic metal cations, where the reaction kinetics are controlled by the exothermicity along with the effect of spin changes. Here, the thermochemistry of the reactions of CO_2 molecules with MO^+ (M = V, Nb, Ta) cations is first discussed. The calculated values of the bond dissociation energy (BDE) of ground-state dioxide cations MO_2^+ (M = V, Nb, Ta), *i.e.* $D_0(OM^+–O)$, at the PBE0-D3(BJ)/def2-TZVP and U/UCCSD(T)/def2-QZVPP levels of theory are summarized in Table 1. Previous thermodynamic information on the $D_0(OM^+–O)$ (M = V, Nb, Ta) from both experimental and theoretical sources are also included for comparison.

Both the PBE0 and U/UCCSD(T) values are consistent with previous measurements and available quantum chemical calculations. Here we adopt the U/UCCSD(T) values of $D_0(OM^+–O)$ with higher accuracy. Combined with the literature thermochemistry of $D_0(OC–O)$ = 526.1 kJ mol^{-1}, reaction (2) is predicted to be exothermic for NbO^+ and TaO^+ cations, while the formation of CO and VO_2^+ dioxide cation from the reaction between the VO^+ cation and CO_2 molecules is considered inefficient, as mentioned earlier. The greater value of $D_0(OTa^+–O)$ than $D_0(ONb^+–O)$ is in reasonable agreement with the rate constants reported by Koyanagi and Bohme that show an increasing trend from NbO^+ to TaO^+ cation. Nevertheless, the discrepancy in reaction kinetics should also be rationalized in terms of the required changes in spin multiplicities.[26]

3.2. Potential energy surface analysis

To further shed light on the difference in reactivity of MO^+ (M = V, Nb, Ta) cations in such spin-nonconserving reactions, potential energy surfaces for the interactions between CO_2 molecules with MO^+ cations at both singlet and triplet spin states are displayed in Fig. 1. The optimized structures of reactants, intermediates, transition states, and products at the PBE0-D3(BJ)/def2-TZVP level are shown in Fig. 2. Using unrestricted methods to calculate multiplet states might introduce spin contamination, potentially reducing the reliability of computed energies and properties. Spin contamination can be quantified by the expectation value of $\langle S^2\rangle$, where $\langle S^2\rangle = S(S+1)$, with S representing the total electron spin quantum number. For an ideal, uncontaminated triplet state, $\langle S^2\rangle$ should theoretically be 2.0. Deviations from this value indicate admixture with other spin states, which can lead to errors in the description of electronic correlation and impact the accuracy of the calculated state energies and properties. The $\langle S^2\rangle$ values for the triplet species listed in Table S1 (ESI†) indicates that spin contamination is minimal and can be reliably neglected in this case. For all three triplet cations, a similar end-on binding situation applies to the triplet reactant complexes (RCs), $^3OM^+$–OCO, formed by dominant electrostatic and orbital interactions.[75] Based on the simplified potential energy curves of different states in Fig. 1, it is expected that all the entrance

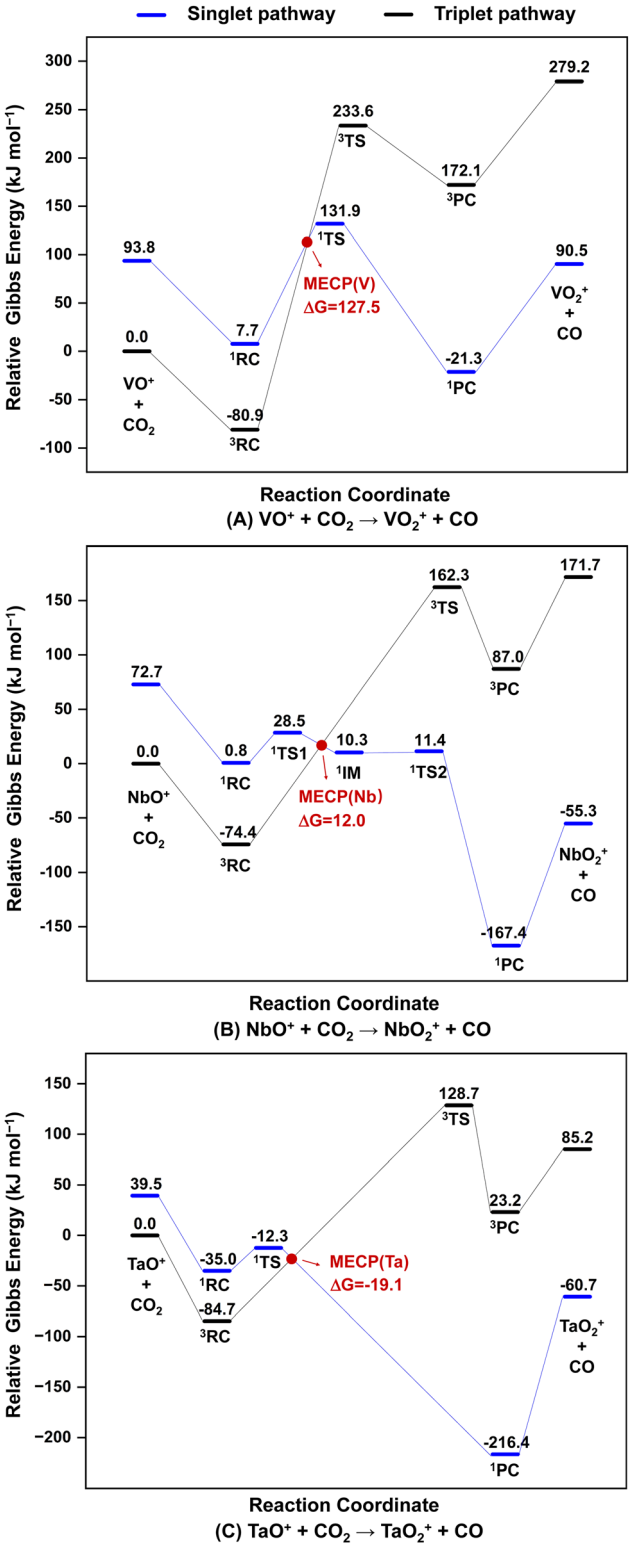

Fig. 1 Reaction pathways for the oxygen atom abstraction by MO^+ (M = V, Nb, Ta) cations on the singlet and triplet energy surfaces calculated at the U/UCCSD(T)/def2-QZVPP level of theory. The relevant complexes are denoted as ^{n}RC (reactant complexes), ^{n}TS (transition states), ^{n}IM (intermediates) and ^{n}PC (product complexes), where n stands for multiplicity. Relative energies are in kJ mol^{-1}.

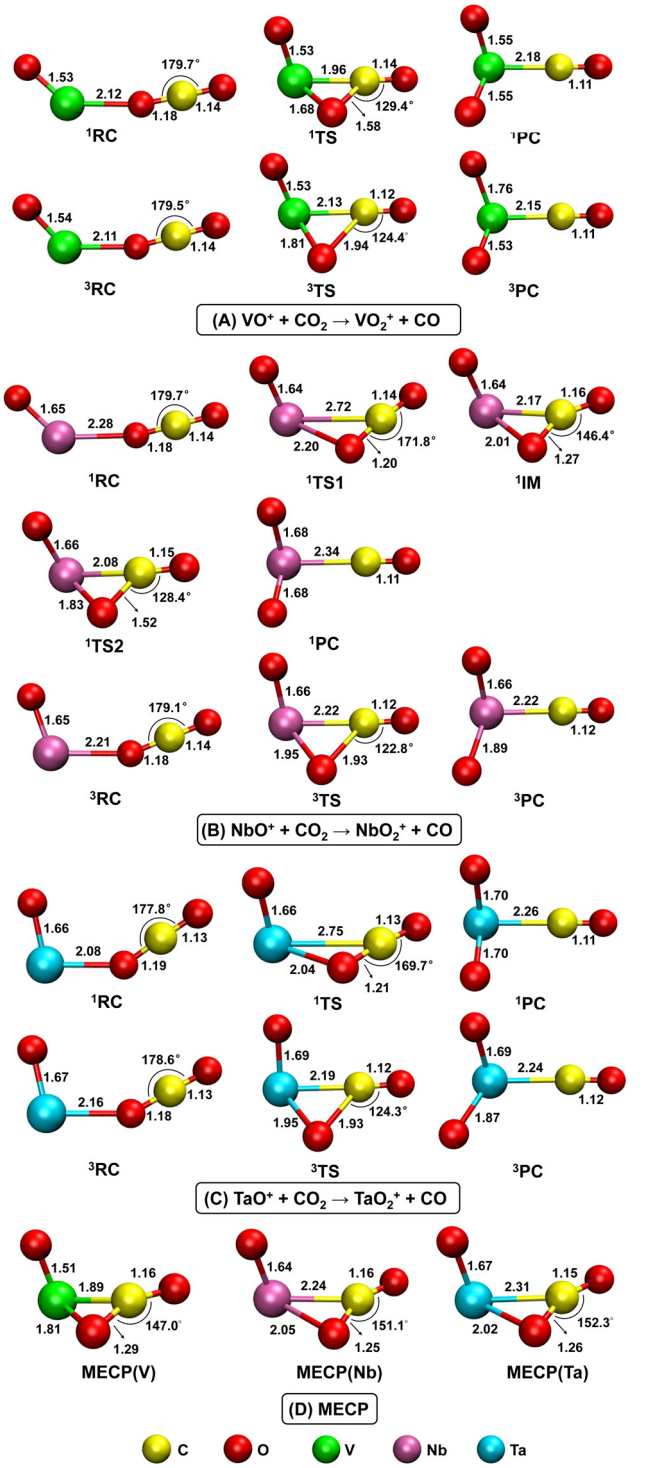

Fig. 2 Optimized structures of reactant complexes, transition states, intermediates, product complexes and minimum energy crossing points for all oxygen atom abstraction reactions on the singlet and triplet energy surfaces calculated at the PBE0-D3(BJ)/def2-TZVP level of theory. Bond lengths are noted in Å.

channels on the ground-state surfaces will evolve onto the singlet surfaces originating from the excited $^1OM^+$–OCO complexes *via* spin crossing points, *i.e.* the minimum energy

crossing points (MECPs).[76,77] After spin inversion at these points, the oxygen atom abstraction from CO_2 molecules by MO^+ cations proceeds along the singlet pathway, ultimately leading to the product channels. Such spin-forbidden reaction routes not only present thermodynamic advantages but also circumvent significantly higher energy barriers associated with triplet surfaces.

From the kinetic consideration expected for a typical two-state reactivity scenario, the rate coefficients of these spin-forbidden reactions are dictated by two electronic factors, *i.e.* the location of the MECP points and the strength of spin–orbit coupling between the singlet and triplet surfaces at MECPs. The positions of MECPs are discussed in the following with emphasis on the height of the crossing regions along with the activation energy barriers. The schematic potential energy curves for the VO^+ cation show that the singlet transition state ^{1}TS, featuring an activated C–O bond distance of 1.58 Å, is located well above the entrance channel by 131.9 kJ mol^{-1}, indicating a high possibility of spin hopping occurring above the reactants level. The corresponding MECP(V) geometry determined between the triplet and singlet surfaces is displayed in Fig. 2(D), with a C–O bond distance (1.29 Å) shorter than that in ^{1}TS. In this regard, the spin crossover through MECP(V) takes place before reaching the singlet transition state ^{1}TS, and subsequently the C–O bond elongates by surmounting the three-member ring ^{1}TS, leading to the generation of the inserted oxocarbonyl product complex (PC) $^1O_2V^+$–CO. A substantial kinetic barrier is therefore expected to impede CO_2 reduction by the VO^+ cation at room temperature, regardless of the surface crossing efficiency. This theoretical finding is in agreement with the absence of observed VO_2^+ cation in gas-phase reactions.[26]

Upon closer inspection of Fig. 1 it is noticed that the NbO^+ cation exhibits a different reaction profile on the singlet surface, characterized by one minimum energy structure (^{1}IM) and two saddle point structures (^{1}TS1 and ^{1}TS2). The two singlet transition states lie above the reactants by 28.5 and 11.4 kJ mol^{-1}, respectively, suggesting that a change in spin multiplicities may occur at an energy level slightly higher than that of the reactants. The structure of MECP(Nb) is located between the first transition state ^{1}TS1 and the intermediate ^{1}IM, as the C–O bond length increasing and the Ta–O bond gradually forming during the oxygen atom abstraction reaction. Accordingly, the singlet transition state ^{1}TS2 with an energy barrier of 11.4 kJ mol^{-1} is accessed after the surface hopping at the MECP(Nb) geometry, followed by the C–O bond cleavage and the formation of $^1O_2Nb^+$–CO complex. The spin crossover at low energy implies that this reaction may proceed without a considerable kinetic barrier and the reaction rate could instead be governed by the spin-forbidden surface crossing process.

In the potential energy diagram for the TaO^+ cation, the singlet transition state ^{1}TS located below the reactants level by −12.3 kJ mol^{-1} presents a greater possibility of experiencing surface crossing with a negligible kinetic barrier. Based on the geometric parameters of the transition states and MECP(Ta), the spin crossover from the triplet to singlet is identified to occur at a region after the singlet transition state ^{1}TS is reached. The corresponding reaction profile reveals a "barrierless" route submerged below the reactants level to produce $^1O_2Ta^+$–CO complex, with the only barrier originating from the spin crossover step. Therefore, the reaction rate of CO_2 molecules with the TaO^+ cation strongly depends on the efficiency of spin inversion at the MECP(Ta) point. However, the activation energy barrier height of this reaction can be only estimated since the MECP is not a stationary point on the potential energy surfaces. This conclusion based on above analysis is in a similar manner to previous assessment of the oxygen atom abstraction reaction of CO_2 with the Ta^+ cation, where the spin-state change, instead of barrier surpassing, is the rate-limiting factor at low reaction energies.[39] The similarity between the two cases lies in the positioning of the crossing seam, which occurs after the saddle points in both instances.

3.3. Analysis of spin–orbit coupling at MECPs

At low kinetic energies with low MECPs, the variations in the rates of the spin crossover steps can be attributed to different spin conversion efficiencies, which is quantitatively described by the magnitude of the root-mean-square spin–orbit coupling matrix element H_{SOC} between the singlet and triplet states at MECPs. As shown in Table 2, the values of H_{SOC} are computed to be 39 cm^{-1} for MECP(V), 160 cm^{-1} for MECP(Nb) and 418 cm^{-1} for MECP(Ta), respectively. The values of the intersystem crossing probabilities are computed to be 0.054 for MECP(V), 0.599 for MECP(Nb) and 0.994 for MECP(Ta), respectively. The significantly large H_{SOC} and P^{ISC} for the spin-forbidden reaction of CO_2 molecules with the TaO^+ cation is indicative of an efficient intersystem crossing, which qualitatively agrees with the experimentally observed increase in rate constant by nearly one order of magnitude than that for the NbO^+ cation. On the other hand, the small H_{SOC} and P^{ISC}in the OV^+–OCO system does not effectively facilitate the crossing of the two potential energy surfaces, which is also consistent with experiment findings.[26]

To further understand the mechanism of intersystem crossing in the present study, an examination on the frontier molecular orbitals of the MECPs at different spin states is conducted. As shown in Fig. 3, the SOMO of the triplet MECPs mainly consists of nonbonding d orbital of metal atoms, which is also the lowest unoccupied molecular orbital (LUMO) of the singlet MECPs. The SOMO-1 of the triplet MECPs reflects the bonding interactions between MO^+ cations and CO_2 parts, which corresponds to the highest occupied molecular orbital (HOMO) of the singlet MECPs. During the transition processes from the triplet state to the singlet state at these MECPs, the spin inversion of the α electron in the SOMO of the triplet MECPs occurs, pairing

Table 2 SOMO and SOMO-1 orbital energy gaps ΔE, spin–orbit coupled coupling constants H_{SOC} and intersystem crossing probabilities P^{ISC} (300 K) for MECP structures

	ΔE (Hartree)	H_{SOC} (cm^{-1})	P^{ISC}
MECP(V)	0.011	39	0.054
MECP(Nb)	0.019	160	0.599
MECP(Ta)	0.026	418	0.994

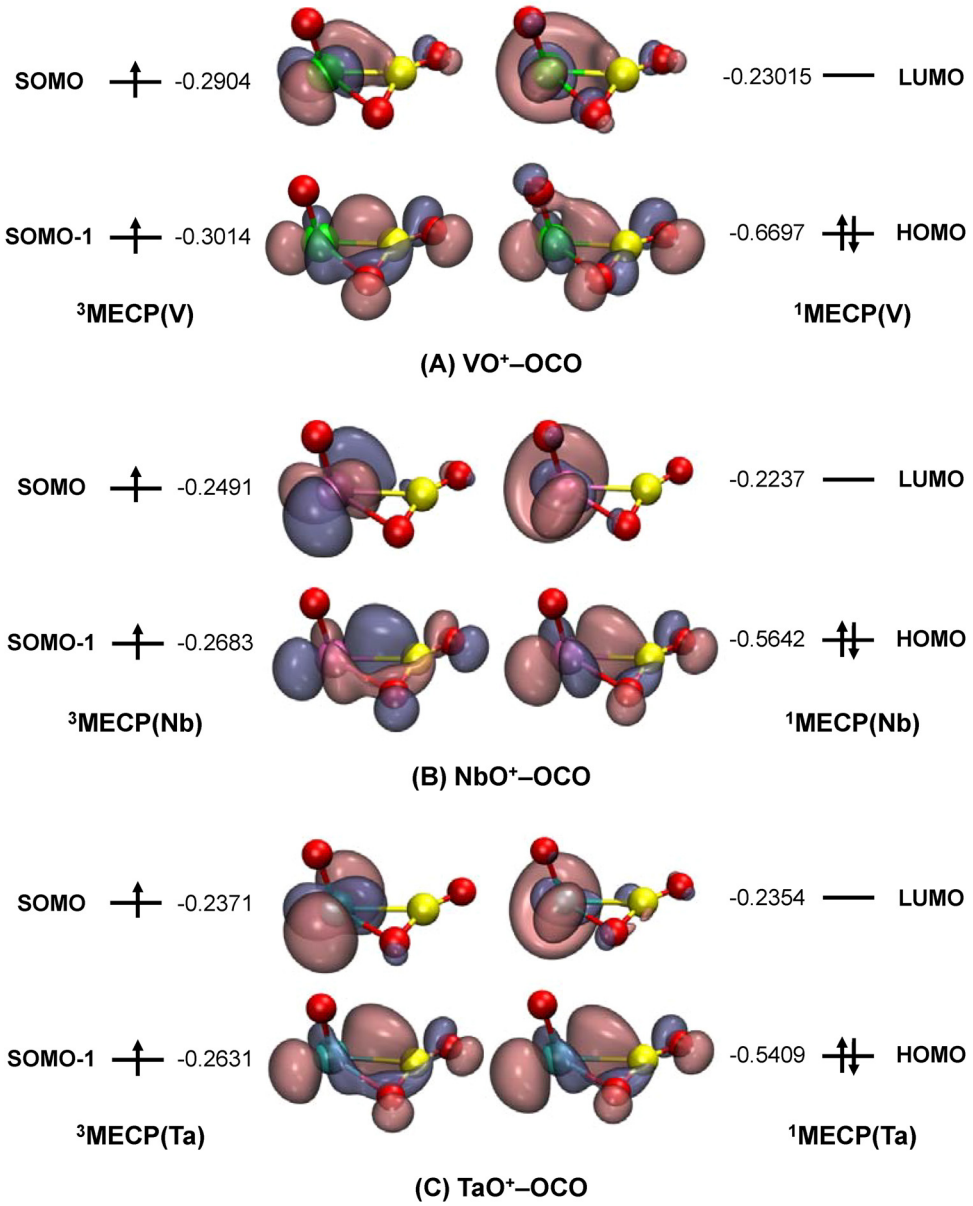

Fig. 3 Diagrams of the frontier molecular orbitals of the MECPs at the singlet and triplet spin states calculated at the ROHF/def2-TZVP level of theory. Orbital energies are shown in Hartree.

Table 3 Contributions from atoms to SOMO and SOMO-1 of the triplet MECPs using natural atomic orbital (NAO) analysis

	Orbitals	Orbital contributions of metal atoms	Shell contributions (>5%) of atoms
MECP(V)	SOMO	90.3%(V)	87.5% 3d(V)
	SOMO-1	51.7%(V)	45.4% 3d(V) + 12.2% 2p(C) + 21.4% 2p(O)
MECP(Nb)	SOMO	94.8%(Nb)	94.8% 4d(Nb) + 6.8% 5s(Nb)
	SOMO-1	58.2%(Nb)	49.9% 4d(Nb) + 6.0% 5s(Nb) + 14.6% 2p(C) + 13.9% 2p(O)
MECP(Ta)	SOMO	98.1%(Ta)	85.6% 5d(Ta) + 11.2% 6s(Ta)
	SOMO-1	59.0%(Ta)	38.3% 5d(Ta) + 17.4% 6s(Ta) + 15.2% 2p(C) + 12.2% 2p(O)

up with β electrons in the SOMO-1. The relative probabilities of spin flipping can be interpreted by evaluating the matrix elements involving molecular orbital angular momentums, which can further be expressed in terms of atomic orbitals. Based on the atomic orbital coefficients of metals atoms in the SOMO and SOMO-1 of the triplet MECPs listed in Table 3, the SOC at

MECPs is likely to increase with higher atomic number of metal atoms. In addition to the shape of molecular orbitals, the energy gap between the orbitals is also responsible for the occurrence of spin flipping at MECPs. As displayed in Table 2, it is evident that the energy gap between the SOMO and SOMO-1 of triplet MECPs rises as the atomic number of metal atoms increases, implying a larger extent of stabilization when α electrons undergoes inversion at triplet MECPs. Overall, the shape along with the energy difference of frontier molecular orbitals play a significant role in determining the intersystem crossing efficiencies between the triplet and singlet reaction pathways at MECPs (Fig. 3).

4. Conclusion

In this study, we presented a thorough theoretical investigation on the gas-phase reaction mechanisms for the reduction of CO_2 to CO by group 5 transition metal monoxide cations from both perspectives of thermodynamics and spin conversion. The exothermic nature of the oxygen atom abstraction from CO_2 molecules was predicted for NbO^+ and TaO^+ cations, whereas endothermic for the VO^+ cation, which is in qualitative agreement with Koyanagi and Bohme's experimental observations.[26] On the basis of potential energy surface analysis, all the reaction mechanisms were revealed to align with the general framework involving two-state reactivity. The reaction between the VO^+ cation and CO_2 molecules is impeded by inefficient intersystem crossing between the triplet and singlet states, as well as the transition state on the singlet-state surface located well above the reactant channel. As the atomic number of the metal atom increases, the efficiency of intersystem crossing becomes the dominant factor influencing the kinetic bottleneck in both cases for NbO^+ and TaO^+ cations, rather than the interplay with energy barriers of transition states. The notably higher values of the spin–orbit coupling matrix element H_{SOC} and the intersystem crossing probability P^{ISC} at the crossing point between the triplet and singlet pathways are calculated for the CO_2 reduction by the TaO^+ cation, providing mechanistic insights into previous experimental findings of a nearly tenfold increase in the rate constant compared to that of the NbO^+ cation.

Data availability

The data supporting this article have been included as part of the ESI.†

Conflicts of interest

The authors declare no conflict of interest.

Acknowledgements

This work was financially supported by the National Natural Science Foundation of China (No. 22403086, 22473104, and 22073088). All DFT calculations were performed on the supercomputing system in the Supercomputing Center of the University of Science and Technology of China.

References

1 L. Cao and K. Caldeira, *Geophys. Res. Lett.*, 2008, **35**, L19609.
2 S. C. Doney, V. J. Fabry, R. A. Feely and J. A. Kleypas, *Ann. Rev. Mar. Sci.*, 2009, **1**, 169–192.
3 M. Tresguerres and T. J. Hamilton, *J. Exp. Biol.*, 2017, **220**, 2136–2148.
4 P. G. Jessop, T. Ikariya and R. Noyori, *Chem. Rev.*, 1995, **95**, 259–272.
5 J. M. Savéant, *Chem. Rev.*, 2008, **108**, 2348–2378.
6 E. E. Benson, C. P. Kubiak, A. J. Sathrum and J. M. Smieja, *Chem. Soc. Rev.*, 2009, **38**, 89–99.
7 W. Wang, S. Wang, X. Ma and J. Gong, *Chem. Soc. Rev.*, 2011, **40**, 3703–3727.
8 C. Finn, S. Schnittger, L. J. Yellowlees and J. B. Love, *Chem. Commun.*, 2012, **48**, 1392–1399.
9 C. Costentin, M. Robert and J.-M. Savéant, *Chem. Soc. Rev.*, 2013, **42**, 2423–2436.
10 J. Qiao, Y. Liu, F. Hong and J. Zhang, *Chem. Soc. Rev.*, 2014, **43**, 631–675.
11 W. Wang, Y. Himeda, J. T. Muckerman, G. F. Manbeck and E. Fujita, *Chem. Rev.*, 2015, **115**, 12936–12973.
12 K. A. Grice, *Coord. Chem. Rev.*, 2017, **336**, 78–95.
13 P. R. Yaashikaa, P. Senthil Kumar, S. J. Varjani and A. Saravanan, *J. CO_2 Util.*, 2019, **33**, 131–147.
14 A. Modak, P. Bhanja, S. Dutta, B. Chowdhury and A. Bhaumik, *Green Chem.*, 2020, **22**, 4002–4033.
15 X. He, Y. Liu, J. Chen, X. Lan, X. Li and S. He, *J. Phys. Chem. Lett.*, 2023, **14**, 6948–6955.
16 S. Saeidi, S. Najari, V. Hessel, K. Wilson, F. J. Keil, P. Concepción, S. L. Suib and A. E. Rodrigues, *Prog. Energy Combust. Sci.*, 2021, **85**, 100905.
17 M. D. Burkart, N. Hazari, C. L. Tway and E. L. Zeitler, *ACS Catal.*, 2019, **9**, 7937–7956.
18 M. D. Porosoff, B. Yan and J. G. Chen, *Energy Environ. Sci.*, 2016, **9**, 62–73.
19 S. Fukuzumi, Y.-M. Lee, H. S. Ahn and W. Nam, *Chem. Sci.*, 2018, **9**, 6017–6034.
20 R. Dobrovetsky and D. W. Stephan, *Angew. Chem., Int. Ed.*, 2013, **52**, 2516–2519.
21 S. Vijay, W. Ju, S. Brückner, S. C. Tsang, P. Strasser and K. Chan, *Nat. Catal.*, 2021, **4**, 1024–1031.
22 A. Fielicke, *Chem. Soc. Rev.*, 2023, **52**, 3778–3841.
23 J. Mascetti, F. Galan and I. Pàpai, *Coord. Chem. Rev.*, 1999, **190–192**, 557–576.
24 L. Zhang, X. Wang, M. Chen and Q. Qin, *Chem. Phys.*, 2000, **254**, 231–238.
25 M. Zhou and L. Andrews, *J. Am. Chem. Soc.*, 1998, **120**, 13230–13239.
26 G. K. Koyanagi and D. K. Bohme, *J. Phys. Chem. A*, 2006, **110**, 1232–1241.

27 S. Lias, J. Bartmess and J. Liebman, *J. Phys. Chem.*, 1988, **17**, 1.
28 J. Herman, J. D. Foutch and G. E. Davico, *J. Phys. Chem. A*, 2007, **111**, 2461–2468.
29 M. R. Sievers and P. B. Armentrout, *J. Chem. Phys.*, 1995, **102**, 754–762.
30 M. R. Sievers and P. B. Armentrout, *Int. J. Mass Spectrom.*, 1998, **179–180**, 103–115.
31 M. R. Sievers, Y. M. Chen and P. B. Armentrout, *J. Chem. Phys.*, 1996, **105**, 6322–6333.
32 P. B. Armentrout and F. Li, *J. Chem. Phys.*, 2004, **121**, 248–256.
33 P. B. Armentrout and J. L. Beauchamp, *Acc. Chem. Res.*, 1989, **22**, 315–321.
34 K. K. Irikura and J. L. Beauchamp, *J. Chem. Phys.*, 1991, **95**, 8344–8351.
35 H. Kang and J. L. Beauchamp, *J. Am. Chem. Soc.*, 1986, **108**, 7502–7509.
36 J. B. Schilling and J. L. Beauchamp, *J. Am. Chem. Soc.*, 1988, **110**, 15–24.
37 E. H. Fowles, J. A. Labinger, J. L. Beauchamp and B. Fultz, *J. Phys. Chem.*, 1991, **95**, 7393–7400.
38 H. Schwarz, *Coord. Chem. Rev.*, 2017, **334**, 112–123.
39 Y. Liu, M. Ončák, J. Meyer, S. G. Ard, N. S. Shuman, A. A. Viggiano and H. Guo, *J. Am. Chem. Soc.*, 2024, **146**, 14182–14193.
40 T. Lu, molclus program, Version 1.9.9.9, **https://www.keyinsci.com/research/molclus.html**, (accessed June 24, 2022).
41 C. Bannwarth, S. Ehlert and S. Grimme, *J. Chem. Theory Comput.*, 2019, **15**, 1652–1671.
42 C. Adamo and V. Barone, *J. Chem. Phys.*, 1999, **110**, 6158–6170.
43 S. Grimme, S. Ehrlich and L. Goerigk, *J. Comput. Chem.*, 2011, **32**, 1456–1465.
44 K. Fukui, *J. Phys. Chem.*, 1970, **74**, 4161–4163.
45 K. Fukui, *Acc. Chem. Res.*, 1981, **14**, 363–368.
46 C. Gonzalez and H. B. Schlegel, *J. Phys. Chem.*, 1990, **94**, 5523–5527.
47 D. G. Truhlar and M. S. Gordon, *Science*, 1990, **249**, 491–498.
48 G. W. T. M. J. Frisch, H. B. Schlegel, G. E. Scuseria, J. R. C. M. A. Robb, G. Scalmani, V. Barone and H. N. G. A. Petersson, *et al.*, *Gaussian, C.01*, Wallingford, CT, 2016.
49 F. Neese, *WIREs: Comput. Mol. Sci.*, 2012, **2**, 73–78.
50 F. Neese, *WIREs: Comput. Mol. Sci.*, 2022, **12**, e1606.
51 J. A. Pople, M. Head-Gordon and K. Raghavachari, *J. Chem. Phys.*, 1987, **87**, 5968–5975.
52 K. Raghavachari, G. W. Trucks, J. A. Pople and M. Head-Gordon, *Chem. Phys. Lett.*, 1989, **157**, 479–483.
53 L. Delgado-Callico, P. Ferrari, J. M. Bakker, F. Baletto and E. Janssens, *Theor. Chem. Acc.*, 2021, **140**, 38.
54 T. Lu, sobMECP program, **https://sobereva.com/286** (accessed April 3, 2023).
55 J. A. Harvey and M. Schwarz, *et al.*, *Theor. Chem. Acc.*, 1998, **99**, 95–99.
56 M. Merchán, L. Serrano-Andrés, M. A. Robb and L. Blancafort, *J. Am. Chem. Soc.*, 2005, **127**, 1820–1825.
57 M. R. Manaa and D. R. Yarkony, *J. Chem. Phys.*, 1991, **95**, 6562–6566.
58 P.-Å. Malmqvist and B. O. Roos, *Chem. Phys. Lett.*, 1989, **155**, 189–194.
59 C. Angeli, R. Cimiraglia and J.-P. Malrieu, *Chem. Phys. Lett.*, 2001, **350**, 297–305.
60 C. Angeli, R. Cimiraglia and J.-P. Malrieu, *J. Chem. Phys.*, 2002, **117**, 9138–9153.
61 S. K. Singh, J. Eng, M. Atanasov and F. Neese, *Coord. Chem. Rev.*, 2017, **344**, 2–25.
62 D. A. Pantazis, X. Chen, C. R. Landis and F. Neese, *J. Chem. Theory Comput.*, 2008, **4**, 908–919.
63 D. A. Pantazis and F. Neese, *J. Chem. Theory Comput.*, 2009, **5**, 2229–2238.
64 J. D. Rolfes, F. Neese and D. A. Pantazis, *J. Comput. Chem.*, 2020, **41**, 1842–1849.
65 T. Lu and F. Chen, *J. Comput. Chem.*, 2012, **33**, 580–592.
66 T. Lu, *J. Chem. Phys.*, 2024, **161**, 082503.
67 T. Lu and F. Chen, *Acta Chim. Sin.*, 2011, **69**, 2393–2406.
68 C. S. Hinton, M. Citir, M. Manard and P. B. Armentrout, *Int. J. Mass Spectrom.*, 2011, **308**, 265–274.
69 J. Han, Y. Yang, B. Qiu, P. Liu, X. Wu, G. Wang, S. Liu and X. Zhou, *Phys. Chem. Chem. Phys.*, 2023, **25**, 13198–13208.
70 J. Han, P. Liu, B. Qiu, G. Wang, S. Liu and X. Zhou, *Dalton Trans.*, 2024, **53**, 171–179.
71 R. C. Bell, K. A. Zemski, D. R. Justes and A. W. CastlemanJr., *J. Chem. Phys.*, 2001, **114**, 798–811.
72 G. K. Koyanagi, D. K. Bohme, I. Kretzschmar, D. Schröder and H. Schwarz, *J. Phys. Chem. A*, 2001, **105**, 4259–4271.
73 J. N. Harvey, M. Diefenbach, D. Schröder and H. Schwarz, *Int. J. Mass Spectrom.*, 1999, **182–183**, 85–97.
74 F. J. Wensink, M. G. Münst, J. Heller, M. Ončák, J. M. Bakker and C. van der Linde, *J. Chem. Phys.*, 2020, **153**, 171101.
75 P. Liu, J. Han, Y. Chen, H. Yu, X. Zhou and W. Zhang, *J. Phys. Chem. A*, 2024, **128**, 3007–3014.
76 D. Schröder, S. Shaik and H. Schwarz, *Acc. Chem. Res.*, 2000, **33**, 139–145.
77 J. N. Harvey, *WIREs: Comput. Mol. Sci.*, 2014, **4**, 1–14.

